



Numerical Study of Surface Plasmon Resonance Biosensor Employing Bismuth Ferrite, Black Phosphorus, and Zinc Telluride for Blood Group Detection

Tanjib Ahmed¹ · Md. Kamal Hosain¹

Received: 14 June 2024 / Accepted: 7 August 2024

© The Author(s), under exclusive licence to Springer Science+Business Media, LLC, part of Springer Nature 2024

Abstract

An optimized prism-based surface plasmon resonance (SPR) sensor, containing a specific material combination, is represented for the accurate detection of the human blood group at a wavelength of 633 nm. The sensor structure includes a BK7 prism as a substrate followed by sequential deposition of silver (Ag), bismuth ferrite (BiFeO₃), black phosphorus (BP), and zinc telluride (ZnTe). The angular interrogation method (ATM) is used to investigate the performance parameters of the sensor, which include sensitivity, detection accuracy, and quality factor. Design and performance analysis is conducted using COMSOL, a finite element method (FEM)-based multiphysics software. Optimization of the thickness of the layers is done to get the highest possible outcome. For resonance and non-resonance conditions, magnetic field propagation and electric field distribution are determined which specifies an enhanced electric field at the metallic layer. The enhanced electric field is produced due to the metallic layer which reflects and redirects the electric field and provides a significant advancement in the performance parameter. The numerical calculations of the sensor parameters are obtained with the sensing medium immobilized with different blood groups (A, B, O). The highest sensitivity, detection accuracy, and quality factor for the detection of blood group A are 298.17 °/RIU, 2.2, and 130.1 RIU⁻¹; for the detection of blood group O are 327.79 °/RIU, 1.98, and 95.35 RIU⁻¹; and for the detection of blood group B are 330.86 °/RIU, 1.73, and 81.33 RIU⁻¹, respectively. The numerical analysis of the sensor parameters assures a significant improvement in the performance compared to previous research studies.

Keywords Blood groups · Surface plasmon resonance · Sensitivity · Black phosphorus · Bismuth ferrite · Zinc telluride

Introduction

Blood group identification is of utmost importance in medical science. The blood groups of patients who have lost a lot of blood must be determined before treating them. It is also essential that the blood groups of the patient and the donor are compatible to avoid a situation of blood incompatibility during the transfusion process [1]. For all blood

transfusions, the “A,” “O,” and “B” blood types are always examined first due to their potent specific antigen-antibody interactions. This is because incompatible blood transfusions can have severe consequences [2]. In biochemical sensing, the surface plasmon-based biosensor has been widely utilized for a few decades. Their distinguishing characteristics including dependability, label-free detection, better sensitivity, and real-time detection capability make them suitable for different sensing applications [3–7]. For sensing applications, various SPR-based sensor configurations comprising optical fiber, grating, prism, and coupled waveguide are developed. In most of the studies, the Kretschmann configuration-based prism biosensor has been examined in which a metal film is deposited on a prism basis [8]. The attenuated total reflection (ATR) phenomenon is followed by the prism-based biosensor [9]. The thin metal layer at the prism-metal interface is penetrated by evanescent waves with exponential attenuation created by the transverse magnetic (TM) polarized input

Tanjib Ahmed and Md. Kamal Hosain contributed equally to this work.

✉ Tanjib Ahmed
tanjibahmed19@gmail.com

Md. Kamal Hosain
khosain@ete.ruet.ac.bd

¹ Department of Electronics & Telecommunication Engineering, Rajshahi University of Engineering & Technology, Rajshahi 6204, Bangladesh

wave [10]. At the interface of the metal-sensing layer, it produces surface plasmon (SP). The resonance angle is affected by changes in the analyte's refractive index (RI) [11].

Conventional SPR-based sensors suffer from some limitations in maximizing performance when analyzing small analyte [12]. These limitations have led researchers to develop multilayer SPR sensors, which greatly improve performance by combining several 2D nanomaterials, perovskite materials, semiconductor materials, and plasmonic materials [13–16]. Moreover, the selection of a low refractive index prism yields enhanced sensitivity and superior performance [17]. Silver (Ag), copper (Cu), aluminum (Al), and gold (Au) are plasmonic metals that are notable for their high SNR ratio, exceptional sensitivity, and a noticeable sharp drop in the SPR curve [18]. Perovskite materials with some exceptional features including a high dielectric constant, ferroelectricity, and piezoelectricity are barium titanate (BaTiO₃), bismuth ferrite (BiFeO₃), potassium niobate (KNbO₃), and lead titanate (PbTiO₃) [18–20]. Biosensors can get benefit from materials with a high dielectric constant [21]. Furthermore, due to their special qualities, two-dimensional (2D) materials including black phosphorus, graphene, and TMDs have drawn attention to SPR prism biosensors. The tunable bandgap and high carrier mobility make it suitable for sensing applications [22, 23]. These materials improve sensitivity in a prism biosensor by increasing effective light-matter interactions at the surface of the sensor. Since 2D materials are thin and atomically layered, precise control over molecular interactions is possible, leading to highly selective biomolecule detection [24–26]. Because of their high refractive index and chemical stability, semiconductor materials like zinc sulfide (ZnS), zinc oxide (ZnO), and zinc telluride (ZnTe) provide a strong SPR effect [9].

Recent studies have explored the use of prism-based SPR sensors for blood group detection. For instance, Raghuwanshi et al. [27] and Pandey et al. [28] explored the use of different metals and prisms in SPR biosensors for blood group identification. Raghuwanshi et al. found that Si prism and Al as the SPR active metal are the best choices providing a sensitivity of 0.117°. Meanwhile, Pandey et al. identified the BK7 prism and used a combination of Ag and Cr as the optimal materials and obtained a sensitivity of 160 °/RIU⁻¹. Both studies emphasized the importance of a buffer layer to prevent oxidation and contamination of blood samples. However, the performance parameters achieved from these biosensors can be enhanced by using different combinations of materials and optimization of the layers. In the proposed work, a multilayer configuration is suggested for detecting the human blood group that utilizes the immense features of BP, BiFeO₃, and ZnSe. This approach effectively overcomes the limitations encountered in prior works, exhibiting superior performance compared to alternative methods. In this work, the sensor structures with various combinations and thicknesses are theoretically studied using the TMM approach. For every

structure optimization, the reflectance curve for various angles of incidence is analyzed. The performance characteristics including angular sensitivity (S), detection accuracy (DA), fixed width at half maximum (FWHM), quality factor (QF), and limit of detection (LOD) are analyzed. This research lead to the development of a quick and precise blood group sensor.

The Design and Modeling of the Proposed Sensor

The configuration of the proposed SPR biosensor for the rapid identification of the human blood group is illustrated in Fig. 1. This is based on the Kretschmann configuration which consists of BK7, Ag, BiFeO₃, BP, and ZnTe. The BK-7 prism is used to improve detection accuracy, quality, and sensitivity. The refractive index of the BK7 prism can be derived from the Sellmeier equation [29]:

$$n_{BK7}^2 = \left(1 + \frac{1.03961212 \times \lambda^2}{\lambda^2 - 0.00600069867} + \frac{0.231792344 \times \lambda^2}{\lambda^2 - 0.0200179144} + \frac{1.001046945 \times \lambda^2}{\lambda^2 - 103.560653} \right) \quad (1)$$

Here, λ indicates the incident electromagnetic wave wavelength.

In this configuration, silver (Ag), bismuth ferrite (BiFeO₃), black phosphorus (BP), and zinc telluride (ZnTe) layers are used.

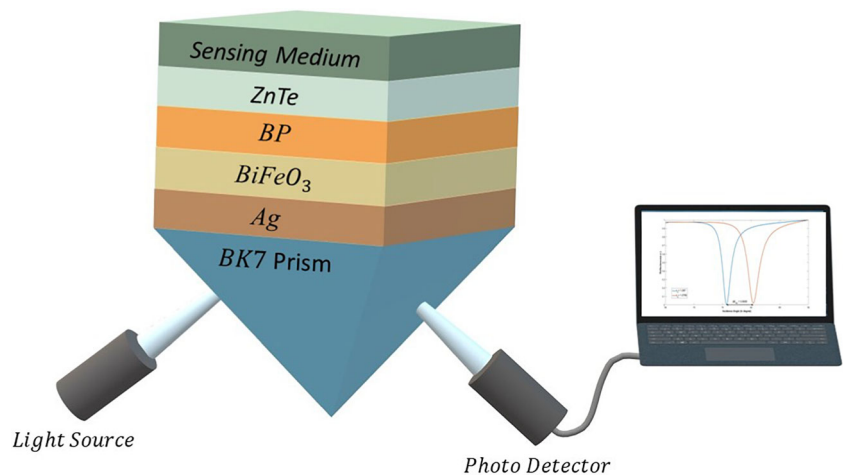
A silver (Ag) layer of 55 nm thickness coated over a coupling prism BK-7. Because of its greater SPR ratio, Ag exhibits better sensitivity as a substrate layer. The lower plasma frequency of Ag makes SPR achievable at longer wavelengths, increasing its versatility for sensing a wider range of biomolecular interactions and analyte concentrations [30]. The refractive index of the silver layer can be derived from the Lorentz-Drude model [31]:

$$n_{Ag}^2 = \left(1 - \frac{\lambda_{cw} \times \lambda^2}{\lambda_{pw}^2 (\lambda_c + i\lambda)} \right) \quad (2)$$

In addition, a bismuth ferrite (BiFeO₃) layer of 0.5 nm thickness is deposited over the silver layer. Due to its potent piezoelectric and ferroelectric properties, the refractive index of the sensor layer is precisely controlled, resulting in increased SPR detection sensitivity. The broad bandgap of BiFeO₃ reduces optical losses, while enhancing the signal-to-noise ratio of the sensor [32]. The refractive index of this material at 633 nm wavelength is 2.9680 [32].

Although employing Ag as a metal in the SPR sensor presents an oxidation problem, the issue is resolved by using

Fig. 1 Schematic illustration of the proposed sensor



2D material. Thus, depositing a BP layer can solve the oxidation problem as it is a 2D material, and with its exceptional electrical qualities increases biomolecule absorption, the sensor is improved by enabling precise control and higher detection [32]. Because of its high sensitivity and adjustable bandgap, BP is a better material to utilize in prism-based SPR sensors than other 2D materials. It offers a unique combination of electrical and optical properties that significantly boost the overall performance and accuracy of SPR sensors. The refractive index of this material at 633 nm of wavelength is $3.5+0.01i$ [32].

Furthermore, ZnTe is deposited on top of the BP layer with a thickness of 5 nm, as it has a higher refractive index and outstanding chemical stability which enables it to give a strong SPR effect [33]. Equation 3 gives the refractive index of ZnTe [34, 35]:

$$n_{ZnTe}^2 = 9.921 + \frac{0.42530}{\lambda^2 - 0.37766^2} + \frac{2.63580}{\frac{\lambda^2}{(56.5)^2} - 1} \quad (3)$$

However, it is moderately toxic, and the toxicity of ZnTe is primarily attributed to the tellurium component [36]. Therefore, it is crucial to handle ZnTe with care and appropriate safety measures. Additionally, when ZnTe is deposited on BP, it is crucial to consider the chemical interactions between the two materials under different environmental conditions, which can affect the stability of BP [37]. Thus, careful consideration in choosing the deposition method is needed to solve this problem. Deposition of ZnTe using the PLD method

Table 1 Refractive index of the corresponding blood group at 633 nm wavelength

Sensing medium	Refractive index
Blood group "A"	1.3739
Blood group "O"	1.3778
Blood group "B"	1.3783

can address this issue by mitigating challenges related to chemical interactions, thermal sensitivity, and material compatibility [38].

Moreover, a sample of blood is drawn as the sensing medium. Based on the experimental findings for the dispersion or refractive index relation of three blood samples, the refractive index of each of the blood groups is indicated by the following Cauchy formula [27]:

$$: n_s(\lambda)|_i = 1.357 + \frac{K_1}{\lambda^2} + \frac{K_2}{\lambda^4} \quad (4)$$

Here, the wavelength of the incident wave λ is in nm, and K_1 and K_2 are the Cauchy coefficients. The subscripts i in Eq. 4 refer to $i = O$, $i = B$, and $i = A$, indicating the blood samples "O," "B," and "A," respectively. Different blood types have different refractive indices followed by Eq. 4 are shown in Table 1. The optical properties of materials with layer thickness employed in the proposed biosensor model are summarized in Table 2, where B and T are considered the number of layers for BiFeO₃ and BP.

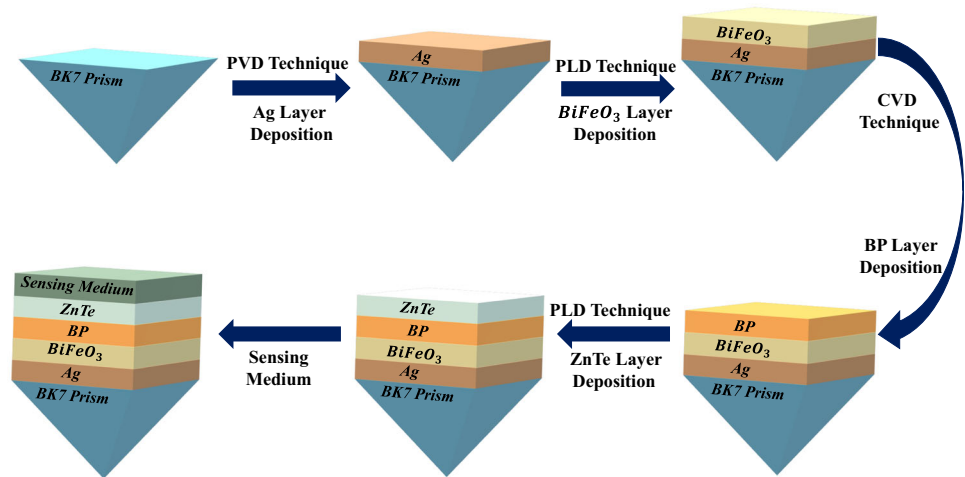
Fabrication Process

The sensor can be realized through the fabrication process depicted in Fig. 2, where it can be constructed by depositing layers of silver, bismuth ferrite, black phosphorus, and

Table 2 Material properties of the sensor layers at 633 nm wavelength

Materials	Refractive index	Thickness	References
Prism (BK7)	1.5151	-	[29]
Silver (Ag)	$0.056206 + 4.2776 \cdot i$	55 nm	[31]
BFO (BiFeO ₃)	2.9680	$B \cdot 0.5$ nm	[32]
Black phosphorus (BP)	$3.5 + 0.01 \cdot i$	$T \cdot 0.5$ nm	[32]
Zinc telluride (ZnTe)	2.9887	3 nm	[34]

Fig. 2 Schematic representation of the fabrication process of the sensor



zinc telluride via appropriate methods. The BK7 prism is to be first soaked in acetone vapor, methanol, and deionized water before the Ag layer is coated. Subsequently, a thermal evaporator system can be employed to deposit metal layers onto the BK7 prism through physical vapor deposition (PVD) [39]. After that, pulsed laser deposition (PLD) utilizes a high-powered laser to vaporize a BFO target, forming a plume that condenses on the underlying silver film, which creates a thin layer of BiFeO₃ with the desired thickness [40]. Then, the BP layer can be fabricated by a conventional chemical vapor deposition (CVD) method and deposited onto the BiFeO₃ nanosheet [41]. Following this, PLD forms ZnTe films on the BP layer by ablating a ZnTe target with a high-powered laser, and the resulting plasma creates a thin film with the desired thickness [38]. To create a functional biosensor, a sensing medium capable of interacting with blood components can be deposited onto the last layer.

Theoretical Background of the Model

Numerical analysis of the sensor is performed to determine the reflectance for a multilayer structure by the use of the transfer matrix approach and the Fresnel equation. Kushwaha et al. [42]. The thickness of each layer varies in the perpendicular direction shown by the z -axis. The boundary conditions at the interfaces of the first and last layers are $Z=Z_1=0$ and $Z=Z_n$, respectively. The dielectric constant of the route layer is equal to the square of its refractive index. These methods use no approximation, allowing them to produce correct findings quickly. The transfer matrix expresses a relationship between the tangential components of electric and magnetic fields of the first and last layers, and the relationship is represented as Eq. 5 [43]:

$$\begin{bmatrix} E_1 \\ H_1 \end{bmatrix} = P \begin{bmatrix} E_{L-1} \\ H_{L-1} \end{bmatrix} \quad (5)$$

Here, E_1 and H_1 are the tangential components of electric and magnetic fields at the first layer contact. The tangential components of electric and magnetic fields at the final layer contact are represented by E_{L-1} and H_{L-1} . P is the characteristic matrix of a multilayer structure with elements P_{ij} , which is defined as follows [43]:

$$P = \prod_{K=2}^{N-1} P_K = \begin{bmatrix} P_{11} & P_{12} \\ P_{21} & P_{22} \end{bmatrix} \quad (6)$$

$$P_K = \begin{bmatrix} \cos \beta_K & \frac{-i}{q_K} \sin \beta_K \\ -iq_K \sin \beta_K & \cos \beta_K \end{bmatrix} \quad (7)$$

Here, K is an arbitrary integer, β_K is the phase thickness, and q_K denotes the refractive indices of the respective layers, as explained by the following [43]:

$$\beta_K = \frac{2\pi d_K}{\lambda} \sqrt{\epsilon_k - n_p^2 \sin^2 \Theta_0} \quad (8)$$

$$q_K = \frac{\sqrt{\epsilon_k - n_p^2 \sin^2 \Theta_0}}{\epsilon_k} \quad (9)$$

where θ_0 is the angle of incidence, λ is the wavelength of the incident light, and n_p is the refractive index of prism. For p-polarized light, the reflection coefficient r is given by the following [43]:

$$r = \frac{(P_{11} + P_{12}q_L)q_1 - (P_{21} + P_{22}q_L)}{(P_{11} + P_{12}q_L)q_1 + (P_{21} + P_{22}q_L)} \quad (10)$$

Finally, the p-polarized light reflectance intensity is represented as follows [43]:

$$r_p = |r|^2 \quad (11)$$

Performance Parameter

To measure the performance of the sensor, some reliable parameters need to be calculated. The performance measurement parameters, such as sensitivity, detection accuracy, FOM, and QF, should be as high as possible to avoid false positive detection [44]. The sensitivity of the sensor utilizing the angular interrogation approach is determined by the change in the SPR point or resonance angle with a change in the RI of the sensing medium. Let the resonance point be identified at Θ_{res}^s and $\Theta_{res}^s + \nabla\Theta_{res}^s$ for the sensing medium refractive index n_s and $n_s + \nabla n_s$, respectively. This indicates the change in the SPR curve due to the alteration in the sensing medium refractive index. The change in refractive index of n_s causes a shift in SPR, defined as $\nabla\Theta_{res}^s$. The performance parameters of the sensor are described below:

The sensitivity (S) is defined mathematically as the ratio of change in the resonance angle (res) to the corresponding change in refractive index (n_s) [45].

$$S = \frac{\nabla\Theta_{res}^s}{\nabla n_s} \quad (12)$$

It is generally expressed in ($^\circ$ /RIU).

The next SPR sensor metric is detection accuracy (DA) or signal-to-noise ratio (SNR). It is given in terms of resonance angle change ($\nabla\Theta_{res}^s$) and FWHM [46].

$$DA = \frac{\nabla\Theta_{res}^s}{FWHM} \quad (13)$$

Here, FWHM defines full width at half maxima.

Another essential parameter of an SPR sensor is the quality factor (QF), which may be expressed in terms of sensitivity (S) and FWHM as follows [46]:

$$QF = \frac{S}{FWHM} \quad (14)$$

It is commonly represented in (RIU⁻¹) units.

Limit of detection (LOD) is the quantitative measurement of the amount of biomolecules or analytes in the sensing medium and is defined as follows [47]:

$$LOD = \frac{\Delta n_s}{\Delta\Theta_{res}^s} \times 0.0573^\circ \quad (15)$$

LOD is computed for extremely slight shifts in the sensing medium. In this analysis, the change is measured for the angular shift of 0.0573° .

The following expression can be used to compute the electric field intensity enhancement factor (EFIEF), which is the

ratio of the square of the electric field at the last interface to the first layer interface [43]:

$$EFIEF = \left| \frac{E\left(\frac{L}{L-1}\right)}{E\left(\frac{1}{2}\right)} \right|^2 = \frac{\varepsilon_1}{\varepsilon_2} \left| \frac{H\left(\frac{L}{L-1}\right)}{H\left(\frac{1}{2}\right)} \right|^2 = \frac{\varepsilon_1}{\varepsilon_2} |t|^2 \quad (16)$$

where t is the transmission coefficient and, ε_1 and ε_L are the respective dielectric constants. The following expression can be used to determine the phase change at resonance angle [42]:

$$\Phi = \arg(r) \quad (17)$$

The dynamic range (DR) is defined as the difference between the maximum and minimum detectable reflections for a specific sensing medium. It can be expressed as follows [48]:

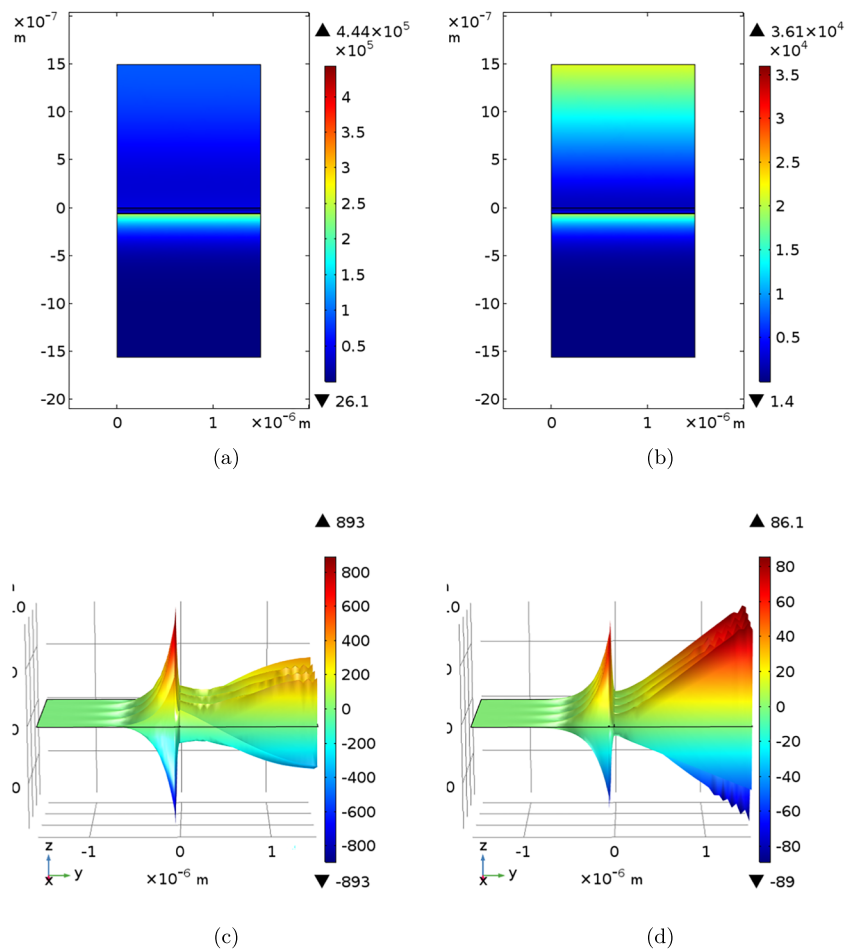
$$\Delta r_n = r_{max} - r_{min} \quad (18)$$

Here, r_{max} is the maximum reflection measured after detection, and r_{min} is the minimum reflection measured before detection.

Computational Setting

COMSOL multiphysics simulation software is used for the design and analysis of the suggested biosensor. When directing light toward the top of the BK7 glass prism, periodic ports in the frequency domain and Floquet periodicity in a periodic condition are selected in the context of electromagnetic waves. The simulation of the SPR biosensor is performed using a frequency domain solver with a frequency of $3 \times 10^8/\lambda$ Hz. For incident angles, a parametric sweep with 0.0573° increments is utilized, encompassing an angle range of 65 to 90° by angular interrogation. The output reflectance intensity curve is used to calculate the resonance angle. Calculations of the sensor performance can be obtained for each relative refractive index of the analytes through the simulation of the fluctuations in the reflectance intensity. Both resonance and non-resonance circumstances are examined in the SPR biosensor inquiry. The magnetic field propagation and electric field intensity are shown in Fig. 3. In the plasmonic layer, significant excitation of surface plasmons and increased localization lead to elevated electric and magnetic field intensities [49]. Electric field intensities for resonance and non-resonance circumstances are shown in Fig. 3 a and b, which indicate that the electric field intensity passes through the metal layer only in the resonance condition. For magnetic field intensities, at a resonance angle, a substantial excitation

Fig. 3 Norm distribution for the electric and magnetic fields. **a** An enhanced electric field with an angle (resonance) of 85.4° . **b** An enhanced electric field with an angle (non-resonance) of 89.6° . **c** An enhanced magnetic field with an angle (resonance) of 85.4° . **d** An enhanced magnetic field with an angle (non-resonance) of 89.6°



in the plasmonic layer is detected. There is no excitation for the non-resonance angle, as seen in Fig. 3 c and d.

Result Analysis

In this study, the SPR biosensor is designed based on the Kretschmann configuration, which includes a prism to give surface plasmons the necessary momentum. The BK-7 prism is chosen due to its low refractive index. By using p-polarized light with a wavelength of 633 nm, SPs can be coupled at the metal-dielectric interface, as shown in Fig. 1. This work focuses on reflectance changes, due to the changes in the sensing medium. The reflectance curve (SPR curve) experiences a noticeable, pronounced dip when resonance is reached. This means that the SPs receive the most energy when resonance conditions are present.

Selection of the Thickness of Silver Layer

It is essential to precisely control the thickness of the metallic layer to achieve the highest excitation of SPs, ideally with

reflectance as close to zero as possible. The silver layer on the BK-7 prism is optimized, as indicated in Fig. 4. A minimal reflectance of 0.0012 at the resonance angle is seen when the silver layer is 55 nm thick. This is explained by a decreased energy loss during the transfer of light from the incident light to the SPs. Notably, the reflectance of the silver layer has a small full width at half maximum (FWHM), which improves the accuracy of detection. The minimal FWHM of 1.335 is achieved with a silver layer thickness of 65 nm. Therefore, a

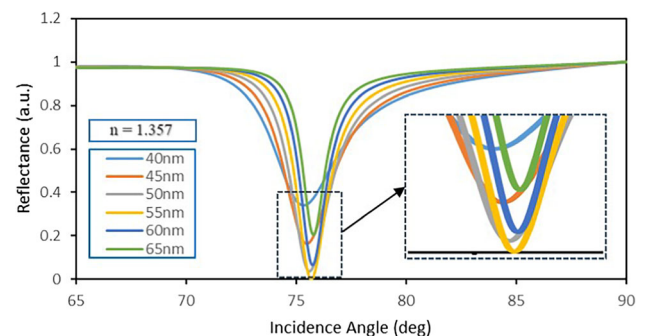


Fig. 4 Variation in reflectance for a range of silver (Ag) thicknesses with respect to the incident angle

Table 3 Different structures of SPR structure

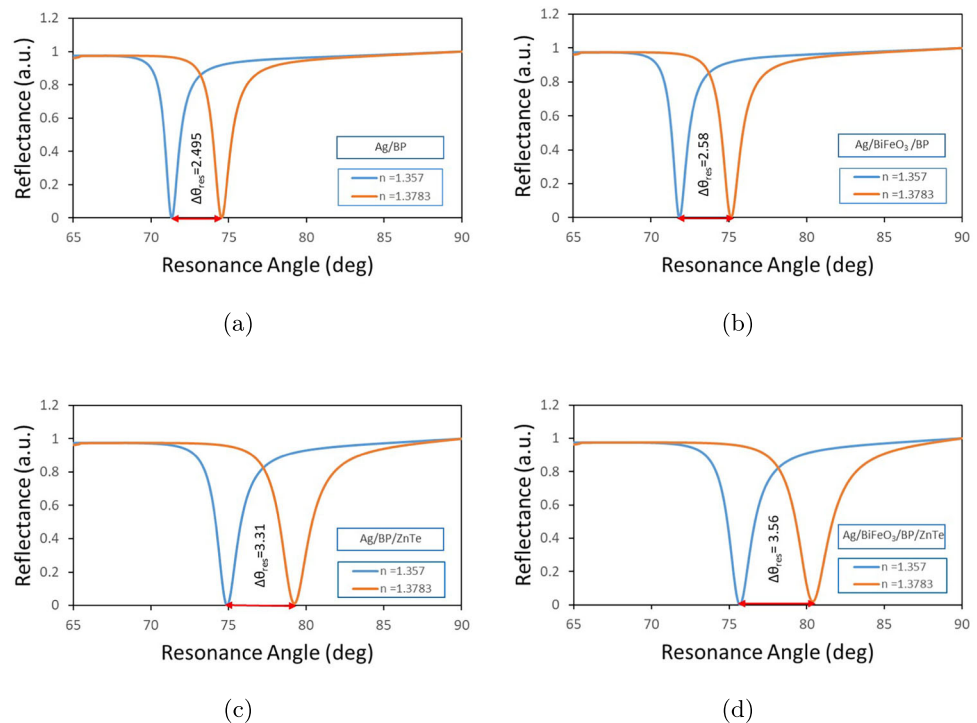
Serial no.	Structures	Design configurations
1	Structure I	BK-7 prism/Ag/BP
2	Structure II	BK-7 prism/Ag/BiFeO ₃ /BP
3	Structure III	BK-7 prism/Ag/BP/ZnTe
4	Structure IV	BK-7 prism/Ag/BiFeO ₃ /BP/ZnTe

trade-off between reflectance and FWHM led to the selection of a 55 nm thickness for the silver layer, yielding reflectance and FWHM values of 0.0012 and 1.78, respectively. Besides, silver only offers a limited amount of chemical stability due to its susceptibility to oxidation. To overcome this oxidation problem, a 2D material BP is considered and it also improves the performance by increasing the absorption quality, since it has a tunable bandgap. The BP layer also includes other distinct characteristics such as exact alignment on the metal coating, expanded surface area, and a high charge carrier density. BiFeO₃ and ZnTe also improve the performance parameter by increasing the absorption capability of the sensor as well as having good chemical stability.

Selection of the Optimal SPR Structure

Different forms of SPR biosensor structures are presented in Table 3 and evaluated in this section. Figure 5 depicts the SPR curve for four distinct configurations applied to the prism.

Fig. 5 Variation of reflectance with respect to incident angle for different SPR configurations. **a** Structure I; $\Delta\theta_{\text{res}} = 2.495^\circ$. **b** Structure II; $\Delta\theta_{\text{res}} = 2.58^\circ$. **c** Structure III; $\Delta\theta_{\text{res}} = 3.31^\circ$. **d** Structure IV; $\Delta\theta_{\text{res}} = 3.56^\circ$



As indicated in Fig. 5a, Structure I includes a two-layer setup with Ag and BP with a thickness of 55 nm and 0.5 nm, respectively, utilizes, and exhibits an SPR angle change of 2.495° with a corresponding sensitivity of $150.4695^\circ/\text{RIU}$. A 2D material, BP is used in SPR sensor designs for solving Ag oxidation problems. This improves sensor performance by providing enhanced control, sensitivity, adjustable bandgap, and increased absorption of biomolecules. Structure II introduces a modified configuration compared to the conventional design. This new structure incorporates a 0.5 nm thick BiFeO₃ layer, along with Ag and BP layers, as depicted in Fig. 5b. In this case, the configuration presents an SPR angle change of 2.58° , and a sensitivity of $155.8685^\circ/\text{RIU}$ is obtained. The strong ferroelectric and piezoelectric characteristics of BiFeO₃ allow for precise adjustment of the refractive index of the layer, which boosts the sensitivity of SPR detection. Moreover, its wide bandgap lowers optical losses as well as improves the signal-to-noise ratio of the sensor. The third scenario which is depicted in Fig. 5c involves Ag, BP, and ZnTe layers with thicknesses of 55 nm, 0.5 nm, and 3 nm, respectively. This structure results in an SPR angle change of 2.58° and a sensitivity of $203.2864^\circ/\text{RIU}$. The addition of the ZnTe layer gives distinct chemical stability and increased refractive index to produce a powerful SPR effect. Finally, Structure IV incorporating Ag, BiFeO₃, BP, and ZnTe layers is demonstrated in Fig. 5d. This structure provides an SPR angle change of 3.56° and a sensitivity of $220.1878^\circ/\text{RIU}$. Hence, among the four structures, Structure IV exhibits the highest sensitivity of $220.1878^\circ/\text{RIU}$. How-

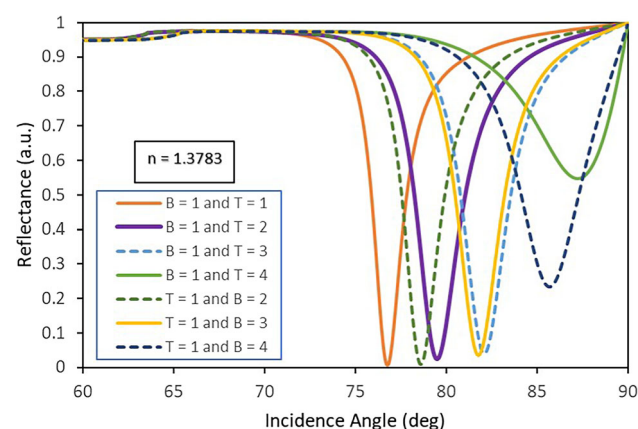
Table 4 Performance parameters for different configurations of the biosensor

Configurations	S ($^{\circ}$ /RIU)	DA	QF (RIU $^{-1}$)
Structure I	150.4695	2.5366	139.8539
Structure II	155.8685	2.4508	135.0199
Structure III	203.2864	2.0973	119.72
Structure IV	220.1878	2.0472	118.2732

ever, The maximum detection accuracy and quality factor of 2.53 and 139.85 RIU $^{-1}$, respectively, are achieved with Structure I. Therefore, a trade-off between detection accuracy, quality factor, and sensitivity led to the selection of the Structure IV as the optimal choice for SPR structure, prioritizing the sensitivity of the biosensor. The selected structure provides sensitivity, detection accuracy, and quality factor of 220.1878, 2.047, and 118.27 $^{-1}$, respectively. Additionally, the overall performance for all structures is summarized in Table 4.

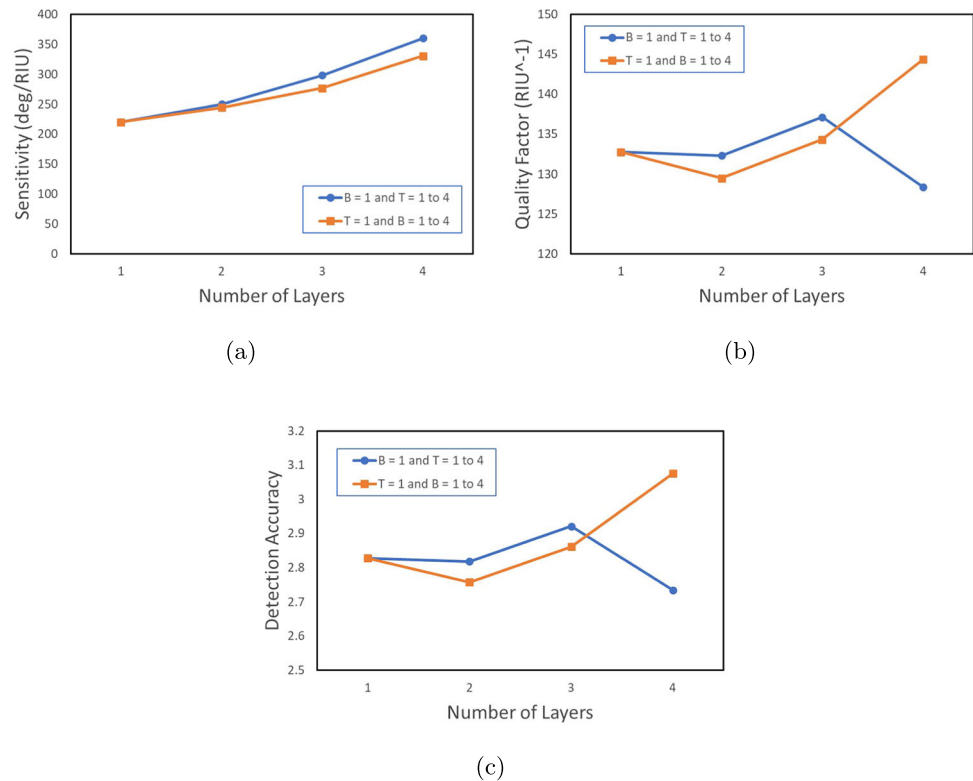
Effect of the Number of BFO and BP Layer

The enhancement of sensitivity and overall performance of the proposed SPR biosensor is intricately linked to the thickness and number of layers of BiFeO $_3$ and BP. The BiFeO $_3$ and BP materials use their distinct characteristics to improve sensor performance. Strong ferroelectric and piezoelectric properties of BiFeO $_3$ enable precise modulation of the refractive index of the sensor layer, hence increasing the sensitivity of SPR detection. The wide bandgap of these materials also reduces optical losses, which raises the signal-to-noise ratio. With its remarkable electrical properties, high sensitivity, tunable bandgap, and enhanced absorption of biomolecules, BP makes a significant contribution to enhanced detection capabilities and more accurate control. Within the sensor


Fig. 6 The variation of the reflectance with respect to the change in the number of BFO and BP layers

configuration, the number of layers is varied from 1 to 4 for both BiFeO $_3$ and BP, while keeping the other layer constant at a single layer. Here, the thickness of each layer of the BiFeO $_3$ and BP is taken as 0.5 nm and 0.5 nm, respectively. Here, B and T indicate the number of layers of BiFeO $_3$ and BP, respectively. The performance of the sensor varies with the changes in the number of layers, which can be attributed to the gradual changes in the FWHM and resonance dip. As the number of layers changes, these parameters show a systematic shift, indicating a direct correlation between the structural configuration and the effectiveness of the sensor. This relationship is clearly illustrated by the reflectance curvature in Fig. 6, where the changes in FWHM and resonance dip with respect to the number of layers are plotted. This graph depicts how the sensor performance is affected by its multilayer structure. The graphical representation in Fig. 7a illustrates the sensitivity (S) variation for the two configurations. A clear positive correlation is observed for the configuration with the increasing number of BiFeO $_3$ layers ($T = 1$ and $B = 1$ to 4). The level of sensitivity grows linearly from a baseline of 220.5753 $^{\circ}$ /RIU ($B = 1$) to a peak of 330.863 $^{\circ}$ /RIU ($B = 4$), highlighting the impact of additional BiFeO $_3$ layers on sensitivity enhancement. On the contrary, a more significant positive correlation is noted when sensitivity is evaluated for the configuration with the increasing number of BP layers ($B = 1$ and $T = 1$ to 4). Sensitivity gradually increases from 220.5753 $^{\circ}$ /RIU ($T = 1$) to 360.4523 $^{\circ}$ /RIU ($T = 4$), indicating a notable improvement associated with a higher number of BP layers. Based on a quality factor (QF) analysis of all the configurations shown in Fig. 7b, the configuration with increment in the BiFeO $_3$ layers ($T = 1$ and $B = 1$ to 4) exhibits a continuous increase in QF, rising from 132.7505 RIU $^{-1}$ ($B = 1$) to 144.3662 RIU $^{-1}$ ($B = 4$). Conversely, after going through an increasing manner from 132.7505 to 137.1386 RIU $^{-1}$, a slight drop in QF is observed for the increment of BP layers ($T = 1$ and $B = 1$ to 4). This decrease is observed from 132.7505 RIU $^{-1}$ ($T = 1$) to 128.3894 RIU $^{-1}$ ($T = 4$). These results suggest that although different BP layers have more complex impacts, additional BiFeO $_3$ layers positively influence QF. Figure 7c shows a slight variation of detection accuracy (DA) for different configurations. DA changes from 2.8276 ($B = 1$) to 3.075 ($B = 4$) when the BiFeO $_3$ layer is varied. Similarly, DA fluctuates very little in the context of BP layer variation (T), falling between 2.8276 ($T = 1$) and 2.7347 ($T = 4$). These results suggest that by changing either the BiFeO $_3$ or the BP layers, the detection accuracy varies with respect to the increasing number of layers in a similar manner to that of the quality factor. However, the highest achieved QF and DA are 144.3662 RIU $^{-1}$ and 3.075, respectively, for 4 layers of BiFeO $_3$ and 1 layer of BP. Therefore, a trade-off between detection accuracy, quality factor, and sensitivity led to the selection of the combination as the optimal choice for SPR

Fig. 7 **a** Sensitivity concerning various BP and BiFeO₃ layer thickness combinations. **b** Detection accuracy concerning various BP and BiFeO₃ layer thickness combinations. **c** Quality factor concerning various BP and BiFeO₃ layer thickness combinations



structure, where the number of the BiFeO₃ layers is four and the BP layer is one. Thus, the final configuration has sensitivity, detection accuracy, and quality factor of 330.863 °/RIU, 3.075, and 144.3662 RIU⁻¹, respectively. Table 5 demonstrates the performance parameters of this optimized sensor.

Analysis of the Dynamic Range

To determine the dynamic range of the proposed sensor, Fig. 8 a and b present SPR curves for ZnTe layer thicknesses ranging from 2.8 to 3.2 nm, before and after detection, respectively. Both figures show a plasmon dip shift with increasing the thickness of the ZnTe layer, while the FWHM also increases in both cases. As a result, detection accuracy declines with the increment of outer layer thickness. Then, the change in reflectance for the variation of outer layer thicknesses is calculated according to Eq. 18, and the resulting curve is plotted in Fig. 9. The curve in Fig. 9 is bell-shaped. The highest reflectance change of 0.9649 is obtained for the sensor with a 3 nm outer layer thickness, which is the dynamic

range of the sensor. A large dynamic range suggests that the sensor exhibits a more substantial response to changes in the sensing medium. Hence, by considering these factors, the optimum thickness of the outer layer is found to be 3 nm.

Variation of Reflectance, Phase, and EFIEF with Incident Angle for Different Blood Group

Figure 10a demonstrates the reflectance curve with respect to the variation of the incidence angle indicating the respective change in the resonance angle for different blood groups. For each blood group as a sensing element, there exhibits minimal reflectivity at the resonance angle. A reduced energy loss during the light transfer from the incident light to the SPs explains this. Notably, a respectable level of detection accuracy is achieved by the minimal FWHM, as shown in Table 5.

The phase interrogation approach, which is mathematically expressed in Eq. 17, has been applied to validate the structure and results. Figure 10b depicts the phase change

Table 5 Performance parameters of the proposed biosensor for blood group detection

Blood group	θ_{SPR} (deg)	$\Delta\theta_{SPR}$ (deg)	FWHM (deg)	S (deg RIU ⁻¹)	DA	QF (RIU ⁻¹)	LOD
A	83.6594	5.042	3.4377	298.1668	2.2	130.1016	1.922×10^{-4}
O	85.4356	6.8182	4.068	327.798	1.9834	95.3539	1.748×10^{-4}
B	85.6647	7.0473	4.1826	330.8592	1.7324	81.3321	1.732×10^{-4}

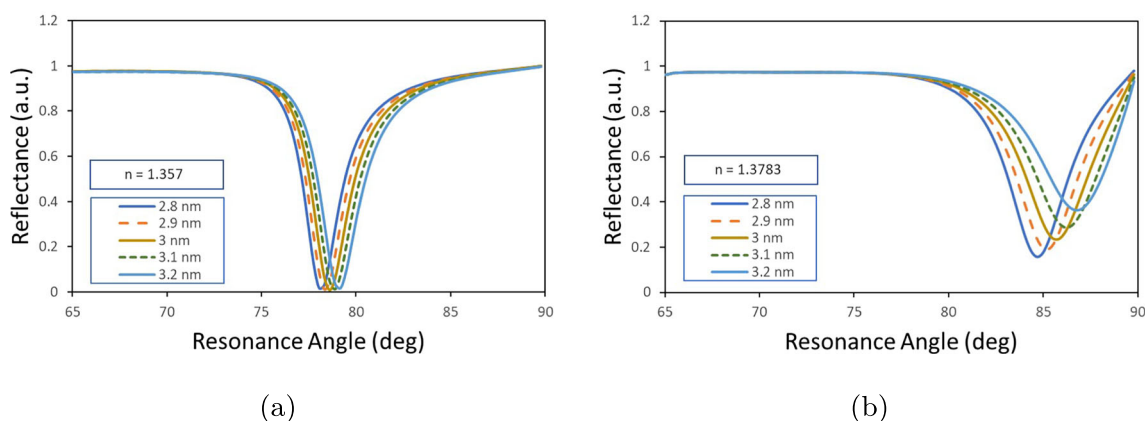


Fig. 8 **a** The variation of the reflectance curve before detection with the variation of ZnTe layer thickness. **b** The variation of the reflectance curve after detection with the variation of ZnTe layer thickness

vs. angle of incidence for the proposed final structure, i.e., (BK7/Ag/BiFeO₃/BP/ZnTe/SM). It has been found that there is a sudden phase change for the varied values of the refractive index of the sensing medium at the same corresponding resonance angle, suggesting different blood groups (A = 1.3739, O = 1.3778, and B = 1.3783). As the refractive index rises, the position of the associated phase change is observed and it shifts toward the higher incidence angle side, suggesting a new blood group. This shift is caused by the structure's surface plasmon damping.

Additionally, an analysis of the relationship between the final structure's electric field intensity enhancement factor (EFIEF) and changes in the refractive index, which indicates various blood groups, is conducted. One important performance metric of the SPR-based biosensor is the EFIEF, which can be computed analytically using Eq. 16. Unlike the metal-dielectric interface, the EFIEF specifies how well the electric field can be confined in the SM. Figure 10c shows the peak

height of the matching field at resonance angles for the optimal construction. Hence, this demonstrates that the SPs are excited at resonance angle when most incident light energy is transmitted to them. Furthermore, it is noted that a drop in EFIEF occurs for each blood type which corresponds with an increase in the refractive index of analyte. This occurs mainly as a result of the gradually stronger absorption of the incident light energy of the analyte.

Electric Field Intensity Analysis

The complex interaction between plasmonic waves and the analyte is illustrated by Fig. 11. Analyte interaction is greatly enhanced by these waves, possessing the unique capacity to increase engagement even with slight variations in the refractive index. Furthermore, Fig. 11 explicitly illustrates that the suggested configuration achieves a notable maximum field intensity of 2.32×10^5 V/m. This highlights the potential of the proposed arrangement for enhanced analytical sensitivity and performance that demonstrates its capacity to produce a strong and concentrated field.

Discussion

The comparative analysis shown in Table 6 illustrates the extent to which the proposed SPR biosensor performs in comparison with the recently published biosensor models. The suggested biosensor exhibits sensitivities of 298.16 °/RIU, 327.798 °/RIU, and 330.859 °/RIU for blood group elements of "A," "O," and "B," respectively, with the highest detection accuracy of 2.2 and a quality factor of 130 RIU^{-1} . In contrast, the sensor designed by Pandey et al. [28] provides a sensitivity of 160 °/RIU, a detection accuracy of 0.75, and a quality

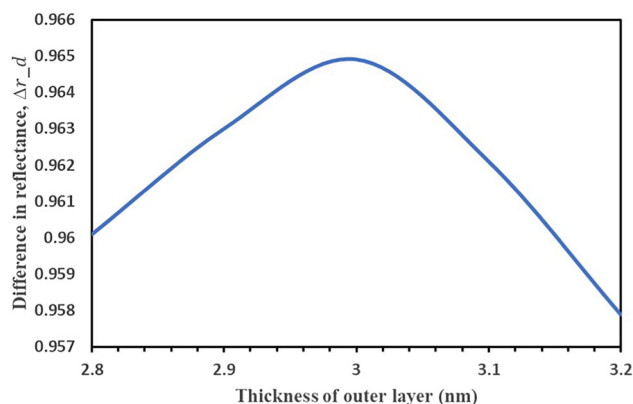
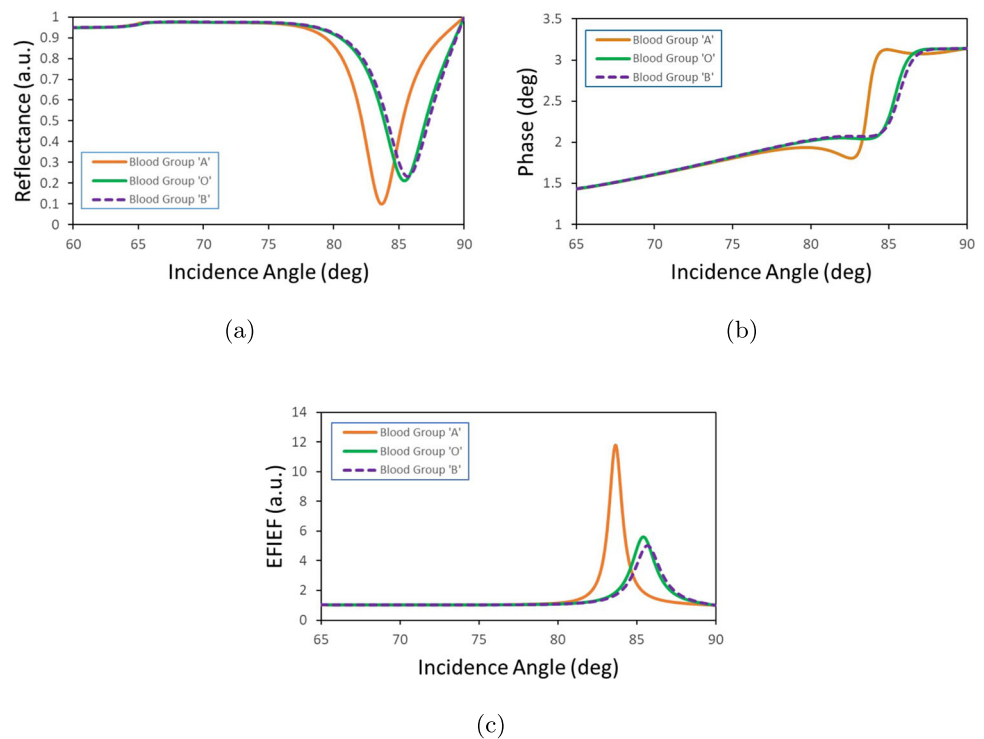


Fig. 9 Variation in the dynamic range with respect to outer layer thickness

Fig. 10 Variation of **a** reflectance, **b** phase, and **c** EFIEF for different RI that correspond to distinct blood types



factor of 115.95 RIU^{-1} . Despite being among the most recent works in SPR sensors for blood group detection, it is outperformed by the current work. However, upon reviewing the performance of other recent SPR sensors, we observe a trend towards higher sensitivity, often at the expense of detection accuracy. For instance, the sensor designed by Roy et al. [50] exhibits a high sensitivity of $402 \text{ }^{\circ}/\text{RIU}$ but has much lower detection accuracy and quality factors of 0.27 and 53.8 RIU^{-1} , respectively. Similarly, the proposed sensor by Singh

et al. [51] demonstrated a moderate sensitivity of $365 \text{ }^{\circ}/\text{RIU}$, but the detection accuracy and quality factor are quite low, at 0.4859 and 94.147 RIU^{-1} , respectively. The sensor designed by Kumar et al. [52] exhibits a moderate sensitivity of $350.76 \text{ }^{\circ}/\text{RIU}$ with a relatively lower detection accuracy of 0.144 and a quality factor of 50.5 RIU^{-1} . Same goes for the proposed sensor of Vasimalla et al. [53] which provides a sensitivity of $321.43 \text{ }^{\circ}/\text{RIU}$ along with a quality factor of 57.09 RIU^{-1} . There are some other works with values of detection accuracy and quality factor close to that of the proposed work but with relatively lower sensitivity. For instance, the sensor designed by Kumar et al. [54] exhibits a quality factor of 100.59 RIU^{-1} , while having a sensitivity of $290.714 \text{ }^{\circ}/\text{RIU}$. Thus, the proposed sensor's combination of high sensitivity and detection accuracy results in a superior quality factor, significantly higher than most of the works mentioned in Table 6. This demonstrates an optimal trade-off between sensitivity and accuracy, which implies that the proposed sensor can not only detect minute changes in refractive index with high precision but also effectively discriminate between different analytes.

Conclusion

SPR biosensors are widely used for biomolecule detection because of their beneficial qualities including fast sensing speeds, short response times, and label-free detection.

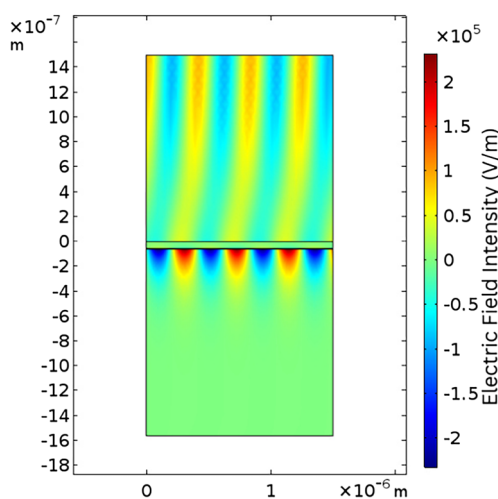


Fig. 11 Inspection of the electric field's intensity for the surface plasmon wave

Table 6 Comparative summary between current work and earlier works

References	Sensor configuration	S (deg RIU ⁻¹)	DA	QF (RIU ⁻¹)
[28]	BK7/Ag/Cr/HfO ₂	160	0.75188	115.95
[54]	BK7/Ag/BaTiO ₃ /Ag/MoS ₂	290.714	0.346	100.59
[53]	BK7/Ag/TiO ₂ /Graphene/BP	321.43	—	57.09
[52]	CaF ₂ /Au/Cu/Franckeite	350.76	0.144	50.5
[51]	BK7/Ag/TiO ₂ /BaTiO ₃ /BP-WS ₂	365	0.4859	94.147
[50]	BAK1 Prism/Ag/WS ₂ /FASnI ₃ /BP	402	0.27	53.8
Current work	BK7/Ag/BiFeO ₃ /BP/ZnTe	330.86	2.2	130.1016

Using a multilayer angular interrogation technique, this work presents the design and analysis of an SPR biosensor for the detection of human blood groups. In the proposed structure, the impact of the BP and the ZnTe layers is analyzed, and precise optimization of the thickness of the layers contributes to the high performance. The sensor provides sensitivities of 298.17 °/RIU, 327.79 °/RIU, and 330.85 °/RIU for blood group samples “A,” “B,” and “O,” respectively, which are superior to the previous works. Furthermore, the detection accuracy of 2.2, 1.98, and 1.73 for blood group samples “A,” “B,” and “O,” respectively, demonstrates its precise detection and reliability. With the ability of rapid and reliable identification of blood group samples, the proposed structure represents a significant advancement in blood type biosensing technology.

Author Contribution Tanjib Ahmed wrote the manuscript text and prepared the figures, while Md. Kamal Hosain provided guidance throughout the process.

Data Availability No datasets were generated or analyzed during the current study.

Declarations

Conflict of Interest The authors declare no competing interests.

References

- Han DJ, Kenmochi T (2023) ABO Incompatibility. In: Gruessner RWG, Gruessner AC (eds) Transplantation of the pancreas, pp 735–754. Springer International Publishing, Cham
- Tangkawsakul W et al (2016) Application of long-range surface plasmon resonance for ABO blood typing. *Int J Anal Chem* 2016
- Homola J, Yee SS, Gauglitz G (1999) Surface plasmon resonance sensors: review. *Sensors Actuators B Chem* 54:3–15
- Borisov SM, Wolfbeis OS (2008) Optical biosensors. *Chem Rev* 108:423–461
- Fan X et al (2008) Sensitive optical biosensors for unlabeled targets: a review. *Anal Chim Acta* 620:8–26
- Wijaya E et al (2011) Surface plasmon resonance-based biosensors: from the development of different SPR structures to novel surface functionalization strategies. *Curr Opin Solid State Mater Sci* 15:208–224
- Kaminski T, Gunnarsson A, Geschwindner S (2017) Harnessing the versatility of optical biosensors for target-based small-molecule drug discovery. *ACS Sens* 2:10–15
- Kretschmann E, Raether H (1968) Notizen: radiative decay of non radiative surface plasmons excited by light. *Z Naturforsch A* 23:2135–2136
- Karki B, Uniyal A, Chauhan B, Pal A (2022) Sensitivity enhancement of a graphene, zinc sulfide-based surface plasmon resonance biosensor with an Ag metal configuration in the visible region. *J Comput Electron* 21:445–452
- Sun J, Du H, Chen Z, Wang L, Shen G (2022) MXene quantum dot within natural 3D watermelon peel matrix for biocompatible flexible sensing platform. *Nano Res* 15:3653–3659
- Xu Y, Wu L, Ang L (2019) Surface exciton polaritons: a promising mechanism for refractive-index sensing. *Phys Rev Appl* 12:024029
- Singh S, Sharma AK, Lohia P, Dwivedi DK (2021) Theoretical analysis of sensitivity enhancement of surface plasmon resonance biosensor with zinc oxide and blue phosphorus/MoS₂ heterostructure. *Optik* 244:167618
- Panda A, Pukhrambam PD (2021) Modeling of high-performance SPR refractive index sensor employing novel 2D materials for detection of malaria pathogens. *IEEE Trans NanoBiosci* 21:312–319
- El-assar M, Taha TE, El-Samie FEA, Fayed HA, Aly MH (2023) ZnSe-based highly-sensitive SPR biosensor for detection of different cancer cells and urine glucose levels. *Opt Quantum Electron* 55:76
- Srivastava T, Jha R, Das R (2011) High-performance bimetallic SPR sensor based on periodic-multilayer-waveguides. *IEEE Photonics Technol Lett* 23:1448–1450
- Singh S et al (2022) Sensitivity enhancement of SPR biosensor employing heterostructure blue phosphorus/MoS₂ and silicon layer. *Emerg Mater Res* 11:239–250
- Srivastava A, Verma A, Das R, Prajapati YK (2020) A theoretical approach to improve the performance of SPR biosensor using MXene and black phosphorus. *Optik* 203:163430
- Srivastava A, Das R, Prajapati YK (2020) Effect of perovskite material on performance of surface plasmon resonance biosensor. *IET Optoelectron* 14:256–265
- Sonia RK, Patel P, Prakash C, Prakash C, Agrawal DK (2012) Low temperature synthesis and dielectric, ferroelectric and piezoelectric study of microwave sintered BaTiO₃ ceramics. *Ceram Int* 38:1585–1589
- Shukla R, Kumar RR, Punetha D, Pandey SK (2023) Design perspective, fabrication, and performance analysis of formamidinium tin halide perovskite solar cell. *IEEE J Photovoltaics*
- Desu SB, Payne DA (1990) Interfacial segregation in perovskites: III, microstructure and electrical properties. *J Am Ceram Soc* 73:3407–3415

22. Karki B, Uniyal A, Sharma T, Pal A, Srivastava V (2022) Indium phosphide and black phosphorus employed surface plasmon resonance sensor for formalin detection: numerical analysis. *Opt Eng* 61:017101–017101
23. Moznuzzaman M, Islam MR, Khan I (2021) Effect of layer thickness variation on sensitivity: an SPR based sensor for formalin detection. *Sens Bio-Sens Res* 32:100419
24. Chemerkouh MJHN, Saadatmand SB, Hamidi SM (2022) Ultra-high-sensitive biosensor based on SrTiO₃ and two-dimensional materials: ellipsometric concepts. *Opt Mater Express* 12:2609–2622
25. Saadatmand SB, Chemerkouh MJHN, Ahmadi V, Hamidi SM (2023) Design and analysis of highly sensitive plasmonic sensor based on 2-D Inorganic Ti-MXene and SrTiO₃ interlayer. *IEEE Sens J* 23:12727–12735
26. Saadatmand SB, Haji Najafi Chemerkouh MJ, Ahmadi V, Hamidi SM (2022) Graphene-based integrated plasmonic sensor with application in biomolecule detection. *J Opt Soc Am B* 40:1–10
27. Raghuwanshi SK, Pandey PS (2022) A numerical study of different metal and prism choices in the surface plasmon resonance biosensor chip for human blood group identification. *IEEE Trans Nanobiosci* 22:292–300
28. Pandey PS, Raghuwanshi SK, Singh R, Kumar S (2023) Surface plasmon resonance biosensor chip for human blood groups identification assisted with silver-chromium-hafnium oxide. *Magnetochemistry* (Basel, Switzerland) 9:21
29. Suresh NV, Rajesh KB, Pillai TVS (2021) Sensitivity enhancement of surface plasmon resonance sensor using Al-Au-BaTiO₃-Graphene layers. *J Opt* 50:152–159
30. Mudgal N, Saharia A, Choure KK, Agarwal A, Singh G (2020) Sensitivity enhancement with anti-reflection coating of silicon nitride (Si₃N₄) layer in silver-based surface plasmon resonance (SPR) sensor for sensing of DNA hybridization. *Appl Phys A* 126:946
31. Shivangani Lohia P, Singh PK, Singh S, Dwivedi DK (2023) Design and modeling of reconfigurable surface plasmon resonance refractive index sensor using Al₂O₃, nickel, and heterostructure BlueP/WSe₂ nanofilms. *J Opt* 52:1358–1369
32. Vasimalla Y, Pradhan HS (2021) A highly performed SPR biosensor based on bismuth ferrite-bromide materials-BP/graphene hybrid structure. *Opt Quantum Electron* 53:695
33. Singh S et al (2023) Theoretical study of malaria detection in blood samples using bimetal layer and zinc telluride nanomaterial-based surface plasmon resonance biosensor. *Plasmonics* 18:2125–2136
34. Li HH (1984) Refractive index of ZnS, ZnSe, and ZnTe and its wavelength and temperature derivatives. *J Phys Chem Ref Data* 13:103–150
35. Marple DTF (1964) Refractive index of ZnSe, ZnTe, and CdTe. *J Appl Phys* 35:539–542
36. Ghosh S, Ghosh D, Bag PK, Bhattacharya SC, Saha A (2011) Aqueous synthesis of ZnTe/dendrimer nanocomposites and their antimicrobial activity: implications in therapeutics. *Nanoscale* 3:1139–1148
37. Ning J (2023) ZnTe-based photodetectors for visible-UV spectral region. In: Korotcenkov G (ed) *Handbook of II–VI semiconductor-based sensors and radiation detectors*, pp 281–300. Springer International Publishing, Cham
38. Kotlyarchuk B, Savchuk V (2007) Investigation of ZnTe thin films grown by pulsed laser deposition method. *Phys Stat Solidi (B)* 244:1714–1719
39. Luna-Moreno D, Sanchez-Alvarez A, Rodriguez-Delgado M (2020) Optical thickness monitoring as a strategic element for the development of SPR sensing applications. *Sensors* 20:1807
40. Zhang G-J, Cheng J-R, Chen R, Yu S-W, Meng Z-Y (2006) Preparation of BiFeO₃ thin films by pulsed laser deposition method. *Trans Nonferrous Metals Soc China* 16:s123–s125
41. Smith JB, Hagaman D, Ji H-F (2016) Growth of 2D black phosphorus film from chemical vapor deposition. *Nanotechnology* 27:215602
42. Kushwaha AS, Kumar A, Kumar R, Srivastava SK (2018) A study of surface plasmon resonance (SPR) based biosensor with improved sensitivity. *Photonics Nanostruct Fundam Appl* 31:99–106
43. Kumar A, Yadav AK, Kushwaha AS, Srivastava SK (2020) A comparative study among WS₂, MoS₂ and graphene based surface plasmon resonance (SPR) sensor. *Sens Actuators Rep* 2:100015
44. Uniyal A, Chauhan B, Pal A, Singh Y (2022) Surface plasmon biosensor based on Bi₂Te₃ antimonene heterostructure for the detection of cancer cells. *Appl Opt* 61:3711–3719
45. Zynio SA, Samoylov AV, Surovtseva ER, Mirsky VM, Shirshov YM (2002) Bimetallic layers increase sensitivity of affinity sensors based on surface plasmon resonance. *Sensors* 2:62–70
46. Sharma AK (2018) Simulation and analysis of Au-MgF₂ structure in plasmonic sensor in near infrared spectral region. *Opt Laser Technol* 101:491–498
47. Pandey AK, Sharma AK (2018) Simulation and analysis of plasmonic sensor in NIR with fluoride glass and graphene layer. *Photonics Nanostruct Fundam Appl* 28:94–99
48. Lan G, Gao Y (2018) Surface plasmon resonance sensor with high sensitivity and wide dynamic range. *IEEE Sens J* 18:5329–5333
49. Dey B, Islam MS, Park J (2021) Numerical design of high-performance WS₂/metal/WS₂/graphene heterostructure based surface plasmon resonance refractive index sensor. *Results Phys* 23:104021
50. Roy S et al (2024) Numerical investigation into impact of halide perovskite material on the optical performance of prism-loaded hybrid surface plasmon resonance biosensor: a strategy to increase sensitivity. *Sens Bio-Sens Res* 43:100630
51. Singh Y et al (2024) Highly sensitive plasmonic biosensor for the detection of Chikungunya virus employing TiO₂ and BP/WS₂ heterostructure. *Plasmonics* 1–9
52. Kumar R et al (2014) Sensitivity enhancement of Franckeite-based surface plasmon resonance sensors using a bimetallic structure. *Plasmonics* 1–8
53. Vasimalla Y et al (2024) Titanium dioxide-graphene-black phosphorus-based SPR sensor for *Helicobacter Pylori* bacteria detection. *IEEE Sens J*
54. Kumar V, Kumar Raghuwanshi S, Kumar S (2024) Highly sensitive Ag/BaTiO₃/MoS₂ nano composite layer based SPR sensor for detection of blood and cervical cancer. *Results Opt* 14:100597

Publisher's Note Springer Nature remains neutral with regard to jurisdictional claims in published maps and institutional affiliations.

Springer Nature or its licensor (e.g. a society or other partner) holds exclusive rights to this article under a publishing agreement with the author(s) or other rightsholder(s); author self-archiving of the accepted manuscript version of this article is solely governed by the terms of such publishing agreement and applicable law.

Terms and Conditions

Springer Nature journal content, brought to you courtesy of Springer Nature Customer Service Center GmbH (“Springer Nature”).

Springer Nature supports a reasonable amount of sharing of research papers by authors, subscribers and authorised users (“Users”), for small-scale personal, non-commercial use provided that all copyright, trade and service marks and other proprietary notices are maintained. By accessing, sharing, receiving or otherwise using the Springer Nature journal content you agree to these terms of use (“Terms”). For these purposes, Springer Nature considers academic use (by researchers and students) to be non-commercial.

These Terms are supplementary and will apply in addition to any applicable website terms and conditions, a relevant site licence or a personal subscription. These Terms will prevail over any conflict or ambiguity with regards to the relevant terms, a site licence or a personal subscription (to the extent of the conflict or ambiguity only). For Creative Commons-licensed articles, the terms of the Creative Commons license used will apply.

We collect and use personal data to provide access to the Springer Nature journal content. We may also use these personal data internally within ResearchGate and Springer Nature and as agreed share it, in an anonymised way, for purposes of tracking, analysis and reporting. We will not otherwise disclose your personal data outside the ResearchGate or the Springer Nature group of companies unless we have your permission as detailed in the Privacy Policy.

While Users may use the Springer Nature journal content for small scale, personal non-commercial use, it is important to note that Users may not:

1. use such content for the purpose of providing other users with access on a regular or large scale basis or as a means to circumvent access control;
2. use such content where to do so would be considered a criminal or statutory offence in any jurisdiction, or gives rise to civil liability, or is otherwise unlawful;
3. falsely or misleadingly imply or suggest endorsement, approval, sponsorship, or association unless explicitly agreed to by Springer Nature in writing;
4. use bots or other automated methods to access the content or redirect messages
5. override any security feature or exclusionary protocol; or
6. share the content in order to create substitute for Springer Nature products or services or a systematic database of Springer Nature journal content.

In line with the restriction against commercial use, Springer Nature does not permit the creation of a product or service that creates revenue, royalties, rent or income from our content or its inclusion as part of a paid for service or for other commercial gain. Springer Nature journal content cannot be used for inter-library loans and librarians may not upload Springer Nature journal content on a large scale into their, or any other, institutional repository.

These terms of use are reviewed regularly and may be amended at any time. Springer Nature is not obligated to publish any information or content on this website and may remove it or features or functionality at our sole discretion, at any time with or without notice. Springer Nature may revoke this licence to you at any time and remove access to any copies of the Springer Nature journal content which have been saved.

To the fullest extent permitted by law, Springer Nature makes no warranties, representations or guarantees to Users, either express or implied with respect to the Springer nature journal content and all parties disclaim and waive any implied warranties or warranties imposed by law, including merchantability or fitness for any particular purpose.

Please note that these rights do not automatically extend to content, data or other material published by Springer Nature that may be licensed from third parties.

If you would like to use or distribute our Springer Nature journal content to a wider audience or on a regular basis or in any other manner not expressly permitted by these Terms, please contact Springer Nature at

onlineservice@springernature.com